# ***Electronic Supplementary Information***

***Physical Measurements***

Elemental analysis (carbon, hydrogen and nitrogen) was performed using a PerkinElmer 240C elemental analyzer. IR spectrum in KBr (4500–400 $cm^{-1}$) was recorded using a PerkinElmer Spectrum Two FT-IR spectrometer. Electronic spectrum in acetonitrile (1000–300 nm) was recorded in a JASCO V-630 spectrophotometer. Fluorescence spectra were obtained on SHIMADZU RF-5301PC Spectrofluorophotometer at room temperature. SQUID magnetometer (Quantum Design MPMS) was used to investigate the magnetic properties (Magnetic susceptibility (Field cooled magnetization/FCM) and M-H measurements). Temperature dependent permittivity over 298 K – 515 K and magneto-dielectric measurements (using an electromagnet supplied by M/S control systems and devices; Mumbai, India) were performed with the Agilent E4980A Precision LCR meter. The polarization study was carried out using Radiant's Precision Premier II ferroelectric tester. Dielectric permittivity and polarizibility were measured by the standard two-probe technique using powdered sample pressed in the form of a pellet with 0.5 $cm^2$ area and 0.06 cm in thickness. Good contact was made by highly conducting silver adhesive and fine copper wires as electrodes.

***Crystal data collection and refinement***

A single crystal having suitable dimensions was used for the X-ray crystallographic analysis using an Agilent Super Nova Dual diffractometer with Atlas detector using mirror-monochromatized Mo-*K*α (λ = 0.71073 Å) radiation at 173 K. CrysAlis Program was used for

the data collection and processing.[2] The intensities were corrected for absorption using the Analytical face index absorption correction method.[3] The structure was solved by charge flipping method with SUPERFLIP.[4] and refined by full-matrix least-squares methods using the WinGX software,[5] which utilizes the SHELXL-97 module.[6] Hydrogen atoms of water molecules were located by difference Fourier maps and were kept fixed. All other hydrogen atoms were placed in their geometrically idealized positions and constrained to ride on their parent atoms.

***Hydrogen bonding interactions***

The hydrogen atom, H(4A) attached with the oxygen atom, O(4), of the lattice water molecule is hydrogen bonded with the oxygen atom, O(6A), of the perchlorate ion. The seccond hydrogen atom, H(4B), attached with the oxygen atom, O(4), of the lattice water molecule, is hydrogen bonded with a symmetry related ($^{\#}$ = -1/4+y,3/4-x,-1/4+z) oxygen atom, O(6A)$^{\#}$, of a second perchlorate anion. A cyclic perchlorate-water octameric $R_8^8(16)$ ring has been produced on repetition of these hydrogen bonding interactions with other symmetry related water molecules and perchlorate ions (Figure S2). This perchlorate-water octamer is hydrogen bonded with the cubane structure to form a three dimensional architecture. The oxygen atom, O(4), of the octameric $R_8^8(16)$ ring is hydrogen bonded with the hydrogen atom, H(2), attached with the nitrogen atom, N(2), of *[Cu(L)]*$^{+}$ unit. On the other hand, the hydrogen atoms, H(3B) and H(3A), attached with N(3) of *[Cu(L)]*$^{+}$ unit are hydrogen bonded with the perchlorate oxygen atoms, O(8A), and O(7A)$^{\Delta}$ (symmetry transformation $^{\Delta}$ = -1/4+y,5/4-x,5/4-z) of two different perchlorate-water $R_8^8(16)$ rings, respectively. The hydrogen bonding interactions are shown in Figure S3. The detail geometric features of hydrogen bonding interactions are given in Table S4.

***IR and electronic spectra***

A distinct band due to azomethine (C=N) group at 1659 $cm^{-1}$ is noticed in infrared spectrum.[7] The sharp, strong, single peak at 1089 $cm^{-1}$ gives evidence for the presence of ionic perchlorate.[8] Sharp bands (doublet), at 3274, 3152 $cm^{-1}$ for the asymmetric and symmetric stretching vibrations, due to the amino $NH_2$ group,[9] has been obscured partially by a broad band at 3379 $cm^{-1}$ indicating the presence of water molecule in the complex (Figure S7).[10]

The electronic spectrum of complex shows two absorption bands at 627 nm and 498 nm in acetonitrile at room temperature. These bands are assigned to the spin allowed transitions $^2B_1g \rightarrow {}^2Eg$ and $^2B_1g \rightarrow {}^2B_2g$ respectively of an octahedral geometry around the copper(II).[11] Third absorption band for the octahedral geometry of copper(II), $^2B_1g \rightarrow {}^2A_1g$, is obscured by a high energy band at 375 nm, which may be assigned as CT band judging from their molar extinction coefficient values (Figure S8).

***Photophysical and powder XRD study***

The luminescence spectrum was obtained in acetonitrile at room temperature. Complex has been photo-exited in UV region (375 nm) which then exhibit fluorescence emission (427 nm and 456 nm) in visible region. The emission bands can be attributed to intra-ligand fluorescent $^1(\pi \rightarrow \pi^*)$ emission of the coordinated ligand (Figure S9).[12]

The experimental powder XRD patterns of the bulk products are in good agreement with the simulated XRD patterns from single crystal X-ray diffraction, indicating consistency of the bulk samples (Figure S10). The simulated patterns of the complexes are calculated from the single crystal structural data (cif files) using the CCDC Mercury software.

***Magnetic properties***

Sample used for magnetic measurements was re-crystallized several times from methanol to get rid of small amounts of impurity, if any. The temperature dependence of the magnetic susceptibility ($\chi$) for the complex measured in the temperature range between 2 and 300 K is shown in Figure 3a. The thermal variation of the product $\chi_M T$ shows the room temperature value around 3.023 $cm^3\ mol^{-1}$ K which is relatively higher than the resultant of four uncoupled spins (S = ½) of copper(II) ions with an anisotropy in *g* value of 2. The decrease of $\chi_M$T value down to 2 K and a maximum appeared in the field cooled magnetization curve simultaneously indicates the existence of dominant antiferromagnetic exchange interactions between the phenoxo bridged copper(II) ions of the cubane core. The magnetization moment appear below 21 K is the resultant moment of the uncompensated spins present in the system which increases at lower temperature when the ordering between them through π-stacking is very weak.

The cubane contains four short and two long Cu···Cu distances, as discussed earlier. The magnetic susceptibility data were simulated introducing two different exchange parameters, *J* (*J* = $J_{12}$ = $J_{13}$ = $J_{42}$ = $J_{43}$) for bridging copper(II) ions and *J* ′ (*J*′ = $J_{14}$ = $J_{23}$) for non-bridging copper(II) ions as shown schematically in Figure S1 using the spin Hamiltonian given by equation (1):

$$\hat{H} = -2J(\hat{S}_{Cu1}\hat{S}_{Cu2} + \hat{S}_{Cu1}\hat{S}_{Cu3} + \hat{S}_{Cu4}\hat{S}_{Cu2} + \hat{S}_{Cu4}\hat{S}_{Cu3}) \\ -2J'(\hat{S}_{Cu1}\hat{S}_{Cu4} + \hat{S}_{Cu2}\hat{S}_{Cu3}) \quad (1)$$

The magnetic susceptibility data for the present complex is fitted in the form of $\chi_M$T vs. T according to the expression given by equation (2) with an additional intercluster interaction term $\theta$ included as mean field correction (Figure 5B). Symbols N, *g*, $\beta$, *k* carry their usual

meanings. $\rho$ is the amount of uncompensated spin moment present at low temperature and $N\alpha$ is the temperature independent paramagnetism (TIP).

$$\chi_m = \frac{2Ng^2\beta^2}{kT} \cdot \frac{A}{B}(1-\rho) + \frac{Ng^2\beta^2}{kT}\rho + N\alpha \qquad (2)$$

where, $A = 2\exp(2J'/kT) + \exp\{(4J' - 2J)/kT\} + 5\exp\{(4J' + 2J)/kT\}$ and $B = 1 + 6\exp(2J'/kT) + \exp\{(4J' - 4J)/kT\} + 3\exp\{(4J' - 2J)/kT\} + 5\exp\{(4J' + 2J)/kT\}$. The best fitted parameters are found to be $J = -40.8$ cm$^{-1}$, $J' = -4.9$ cm$^{-1}$, $g = 2.12$, $\rho = 5.1$ %, $\theta = +0.28$ K and $N\alpha = 3.5 \times 10^{-4}$ emu mol$^{-1}$ respectively, where $R^2 = 5.8 \times 10^{-5}$ ( $\sum T^2(\chi_{obs} - \chi_{cal})^2 / \sum T^2(\chi_{obs})^2$ ).

The exchange interaction (J) between the four short Cu···Cu pairs (3.281 Å) mainly takes place through the relatively shorter Cu–O–Cu bond pathways with 1.988 and 1.951 Å present at one side of the two bridges. The exchange coupling occurred between the short Cu···Cu pairs (J) in perfect [4+2] cubane (four short and two long Cu···Cu distances) is both ferromagnetic as well as antiferromagnetic depending on the Cu–O–Cu angle (β).[13,14] In our case, the presence of larger Cu–O–Cu angle (β = 112.8°) into short Cu–O–Cu pathways becomes dominant factor for the negative exchange coupling (J = –40.8 cm$^{-1}$) ensuing antiferromagnetic interaction instead of ferromagnetic interaction. The large value of τ (~49.5°) increases the bridged Cu–O distance ($d_1$) as a result of distortion which results weak antiferromagnetic exchange interaction (J) due to poor overlapping between orbitals of bridged copper(II).[15-17] Similar bond lengths (1.988 and 2.671 Å) and bond angles (93.5°) are present for the J exchange pathway at both sides of the unbridged long Cu···Cu pairs (3.410 Å). Tercero et al. showed that the J exchange interaction becomes weak with increase in axial bond distance ($d_2$) for the [4+2] (four short and two long

Cu···Cu distances) cubane core.[14] Due to Jahn-Teller effect, axial Cu-O bonds get elongated and as a result the half filled $d_{x2-y2}$ orbitals of each copper(II) at the sides of unbridged long Cu···Cu pairs become away from each other and hence less superexchange coupling exists between the parallel $d_{x2-y2}$ orbitals. Therefore, although the small Cu–O–Cu angle ($\alpha$ = 93.5°) gives ferromagnetic exchange, the presence of very long axial Cu–O distance ($d_2$ = 2.671 Å) shows weak antiferromagnetic exchange interaction with $J' = -4.9\ cm^{-1}$.

## References


1. S.-L. Li, D.-X. Liu, J.-H. Zhou and F.-Q. Meng, *Chin. J. Struct. Chem.*, 1995, **14**, 88.

2. CrysAlisPro, Agilent Technologies. Version 1.171.36.21 (2012).

3. R. C. Clark and J. S. Reid, *ActaCryst.*, 1995, **A51**, 887-897.

4. L. Palatinus and G. Chapuis, *J. Appl. Cryst.*, 2007, **40**, 786-790.

5. L. J. Farrugia, *J. Appl. Cryst.*, 1999, **32**, 837-838.

6. G. M. Sheldrick, *ActaCryst.*, 2008, **A64**, 112-122.

7. M. Das, S. Chatterjee, K. Harms, T. K. Mondal and S. Chattopadhyay, *Dalton Trans.*, 2014, **43**, 2936–2947.

8. M. Das and S. Chattopadhyay, *Polyhedron*, 2013, **50**, 443–451.

9. M. Das, S. Chatterjee and S. Chattopadhyay, *Polyhedron*, 2014, **68**, 205–211.

10. M. Das, K. Harms and S. Chattopadhyay, *Dalton Trans.*, 2014, **43**, 5643–5647.

11. C. Biswas, S. Chattopadhyay, M. G. B. Drew, A. Ghosh, *Polyhedron*, 2007, **26**, 4411–4418.

12. M. Das, B. N. Ghosh, K. Rissanen and S. Chattopadhyay, *Polyhedron*, 2014, **77**, 103-114.

13. E. Ruiz, P. Alemany, S. Alvarez and J. Cano, *J. Am. Chem. Soc.*, 1997, **119**, 1297−1303.

14. J. Tercero, E. Ruiz, S. Alvarez, A. Rodriguez-Fortea and P. Alemany, *J. Mater. Chem.*, 2006, **16**, 2729−2735.

15. V. H. Crawford, H. W. Richardson, J. R. Wasson, D. J. Hodgson and W. E. Hatfield, *Inorg. Chem.*, 1976, **15**, 2107-2110.

16. E. Ruiz, P. Alemany, S. Alvarez and J. Cano, *Inorg. Chem.*, 1997, **36**, 3683-3688.

17. S. Thakurta, P. Roy, R. J. Butcher, M. S. E. Fallah, J. Tercero, E. Garribba and S. Mitra, *Eur. J. Inorg. Chem.*, 2009, 4385–4395.

**Table S1:** Selected bond angles (º) around copper(II) for the complex.

| | | | |
|---|---|---|---|
| O(1)-Cu(1)-O(3) | 170.04(14) | O(3)-Cu(1)-N(1) | 81.44(15) |
| O(1)-Cu(1)-O(1)* | 84.10(14) | O(1)*-Cu(1)-O(1)^ | 70.33(13) |
| O(1)-Cu(1)-O(1)^ | 88.20(14) | O(1)*-Cu(1)-O(2)^ | 145.94(11) |
| O(1)-Cu(1)-O(2)^ | 99.35(14) | O(1)*-Cu(1)-N(1) | 103.42(13) |
| O(1)-Cu(1)-N(1) | 91.51(15) | O(1)^-Cu(1)-O(2)^ | 75.90(14) |
| O(3)-Cu(1)-O(1)* | 90.68(14) | O(1)^-Cu(1)-N(1) | 173.73(16) |
| O(3)-Cu(1)-O(1)^ | 98.04(14) | O(2)^-Cu(1)-N(1) | 110.31(14) |
| O(3)-Cu(1)-O(2)^ | 89.73(15) | - | - |

Symmetry transformations: * = 1-x,1/2-y,z; ^ = 3/4-y,-1/4+x,7/4-z

**Table S2:** Geometric features (distances in Å and angles in °) of the π···π stacking

| Cg(Ring I)···Cg(Ring J) | Cg(I)···Cg(J) | α | Cg(I)···Perp | Cg(J)···Perp | Slippage |
|---|---|---|---|---|---|
| Cg(24)···Cg(24) | 3.645(3) | 0 | 3.591(2) | 3.591(2) | 0.628 |

α = Dihedral Angle between ring I and ring J; Cg(I)···Perp = Perpendicular distance of Cg(I) on ring J; Cg(J)···Perp = Perpendicular distance of Cg(J) on ring I; Cg(24) = Centre of gravity of the ring $\mathbf{R^{24}}$ [N(3)–C(12)–C(13)–C(14)–C(15)–C(16)].

**Table S3:** Variation in coercivity values of the magnetic hysteresis curves both in +ve and –ve magnetic fields at various temperatures.

| **Temperature (K)** | | **2** | **4** | **7** | **10** | **20** | **30** | **50** | **300** |
|---|---|---|---|---|---|---|---|---|---|
| **Coercivity (Oe)** | +ve Field | 705 | 590 | 1090 | 960 | 1930 | 980 | 510 | 160 |
| | –ve Field | 805 | 610 | 980 | 960 | 1870 | 1570 | 570 | 165 |

**Table S4:** Hydrogen bond distances (Å) and angles (º) for the complex.

| D–H···A | D–H | D···A | H···A | ∠D–H···A |
|---|---|---|---|---|
| N(2)–H(2)···O(4) | 0.881(5) | 2.821(9) | 1.982(8) | 158.8(4) |
| N(3)–H(3A)···O(7A)$^{\Delta}$ | 0.880(6) | 3.17(2) | 2.37(2) | 150.9(5) |
| N(3)–H(3B)···O(8A) | 0.880(6) | 3.29(2) | 2.43(2) | 163.9(6) |
| O(4)–H(4A)···O(6A) | 0.848(9) | 2.96(1) | 2.20(1) | 149.3(6) |
| O(4)–H(4B)···O(6A)$^{\#}$ | 0.840(8) | 2.99(2) | 2.15(1) | 176.9(6) |

Symmetry transformations: $^{\Delta}$ = -1/4+y,5/4-x,5/4-z; $^{\#}$ = -1/4+y,3/4-x,-1/4+z. D, donor; H, hydrogen; A, acceptor

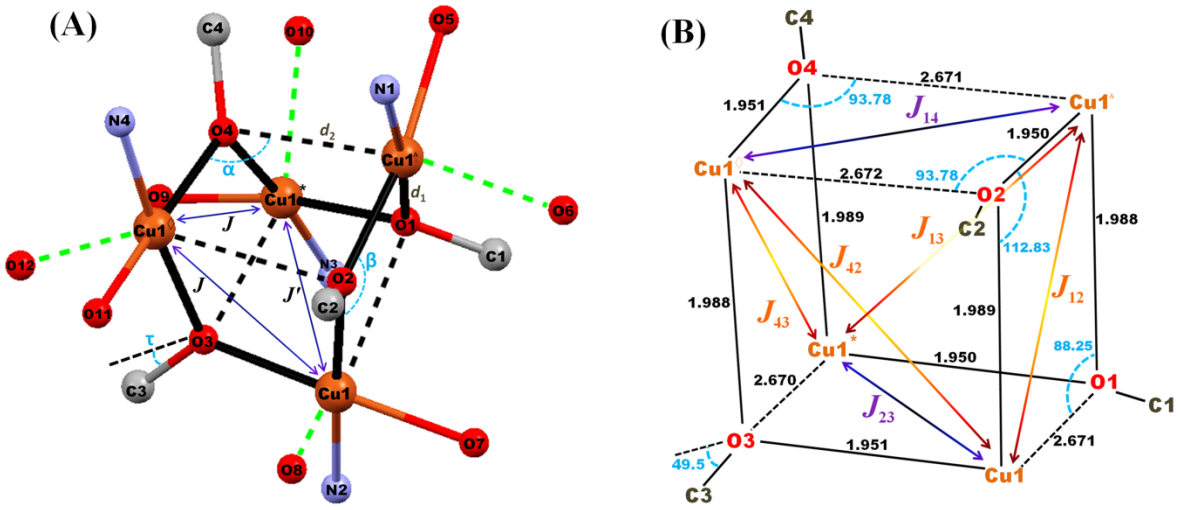


**Figure S1:** (**A**) Defines the bond lengths ($d_1$, $d_2$) and angles (α,β,τ) related to exchange coupling interactions ($J$ and $J'$) within the intracubane. (**B**) Represents the values of corresponding bond lengths and angles with the exchange coupling terms ($J_{12} = J_{13} = J_{42} = J_{43} = J$ and $J_{14} = J_{23} = J'$) between each bridged dicopper atoms.

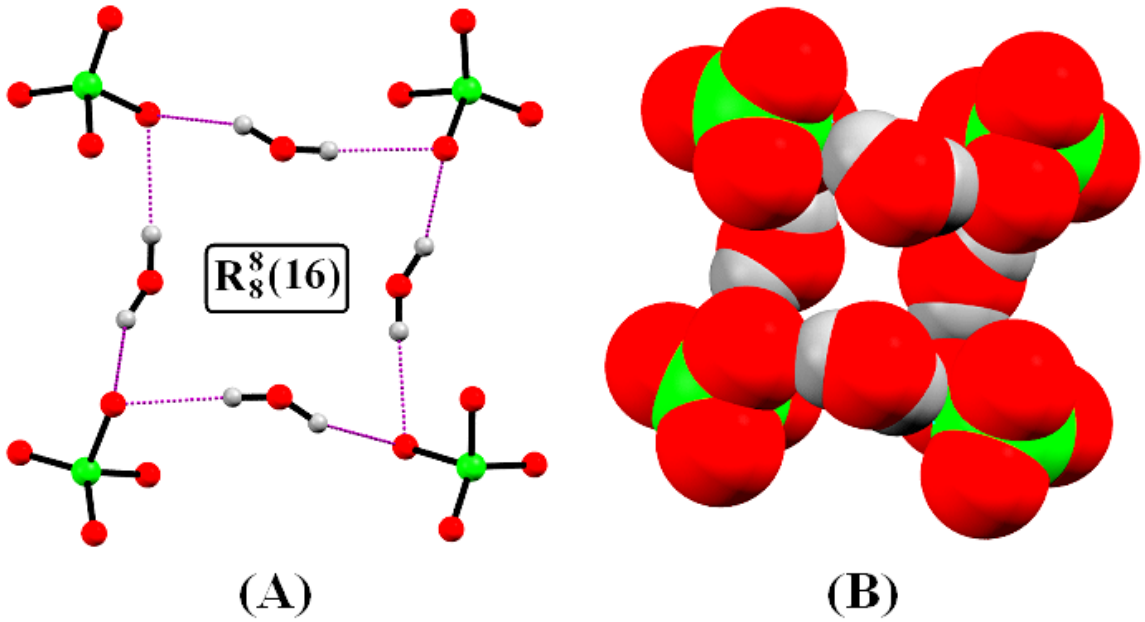


**Figure S2:** A perspective view of (**A**) hydrogen bonding interactions within perchlorate-water octameri ring, $R_8^8(16)$ and (**B**) its spacefill model representation.

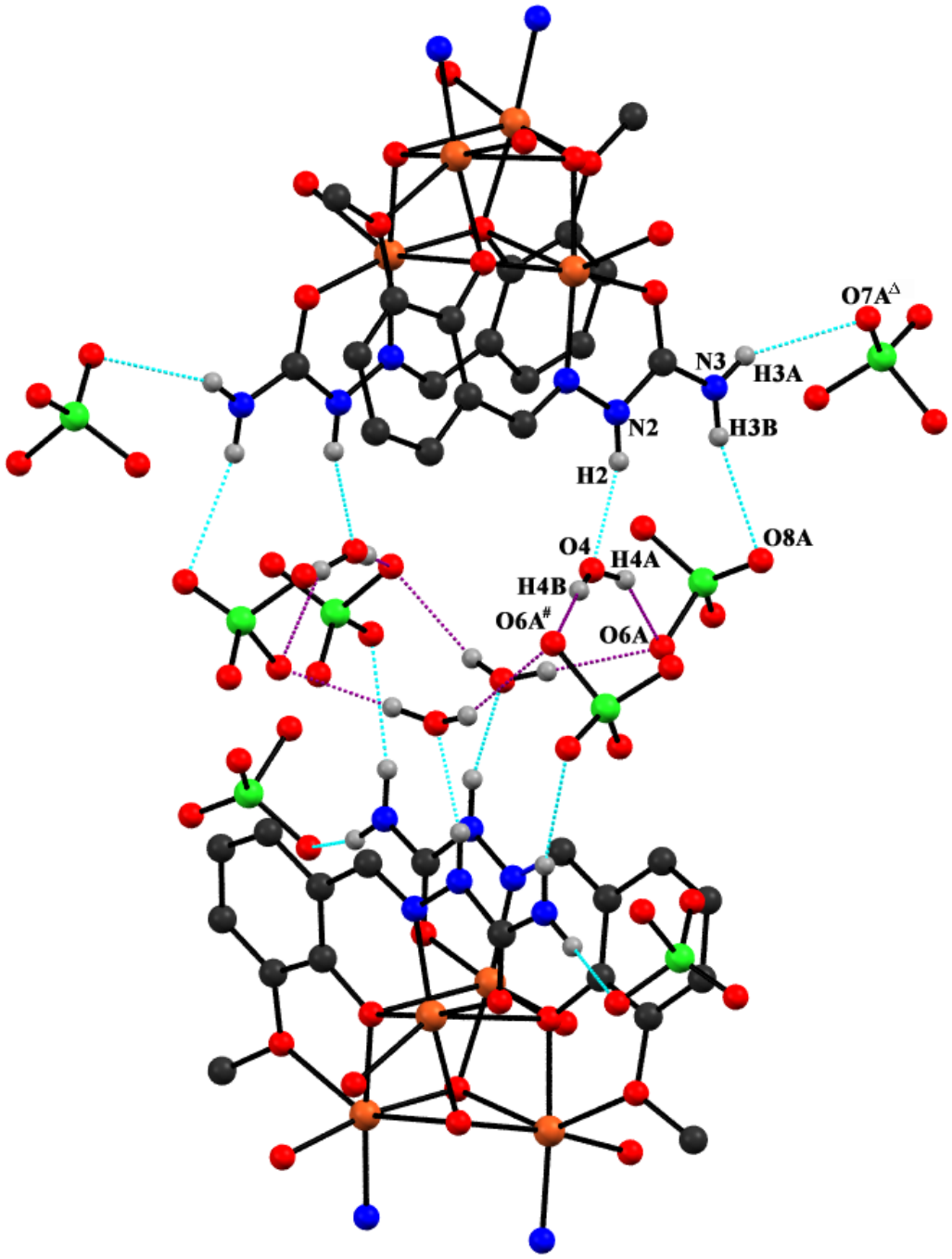


**Figure S3:** A perspective view of host-guest interaction of cyclic perchlorate-water octamer, $R_8^8(16)$, guest with complex host.

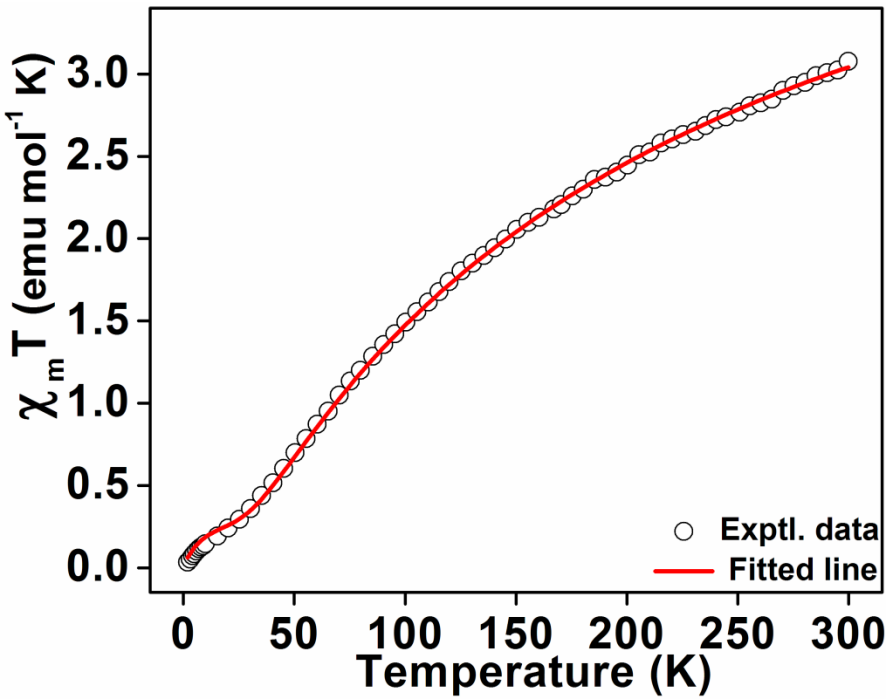


**Figure S4:** Variation of $\chi_M T$ with T. The solid line (red colour) represents the best fit curve.

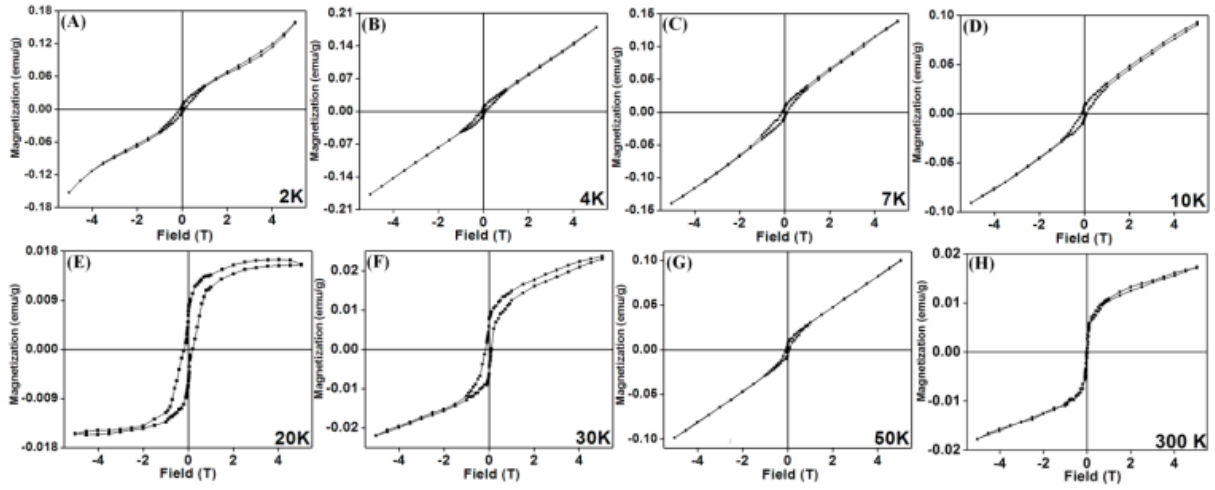


**Figure S5:** Unusual behavior of magnetization (A–H) as a function of magnetic field at different temperatures showing the perfect ferromagnetic ordering at 20 K (E) with highest coercivity of ~2000 Oe.

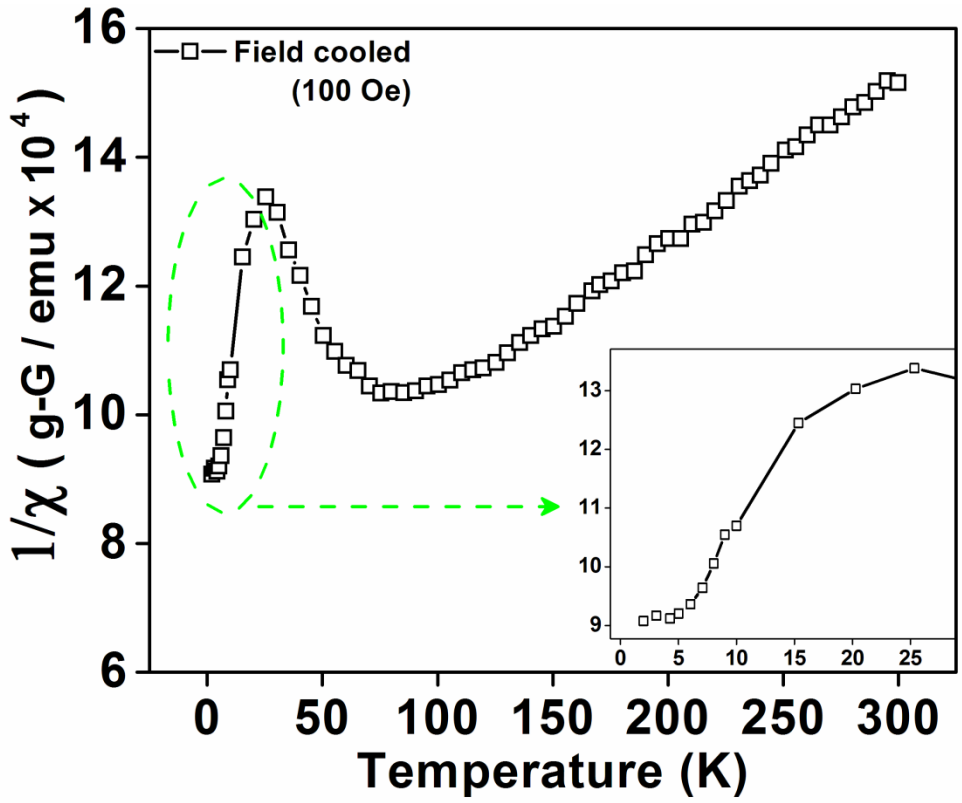


**Figure S6:** Thermal variation of 1/χ (*1/χ vs T plot*) for the complex.

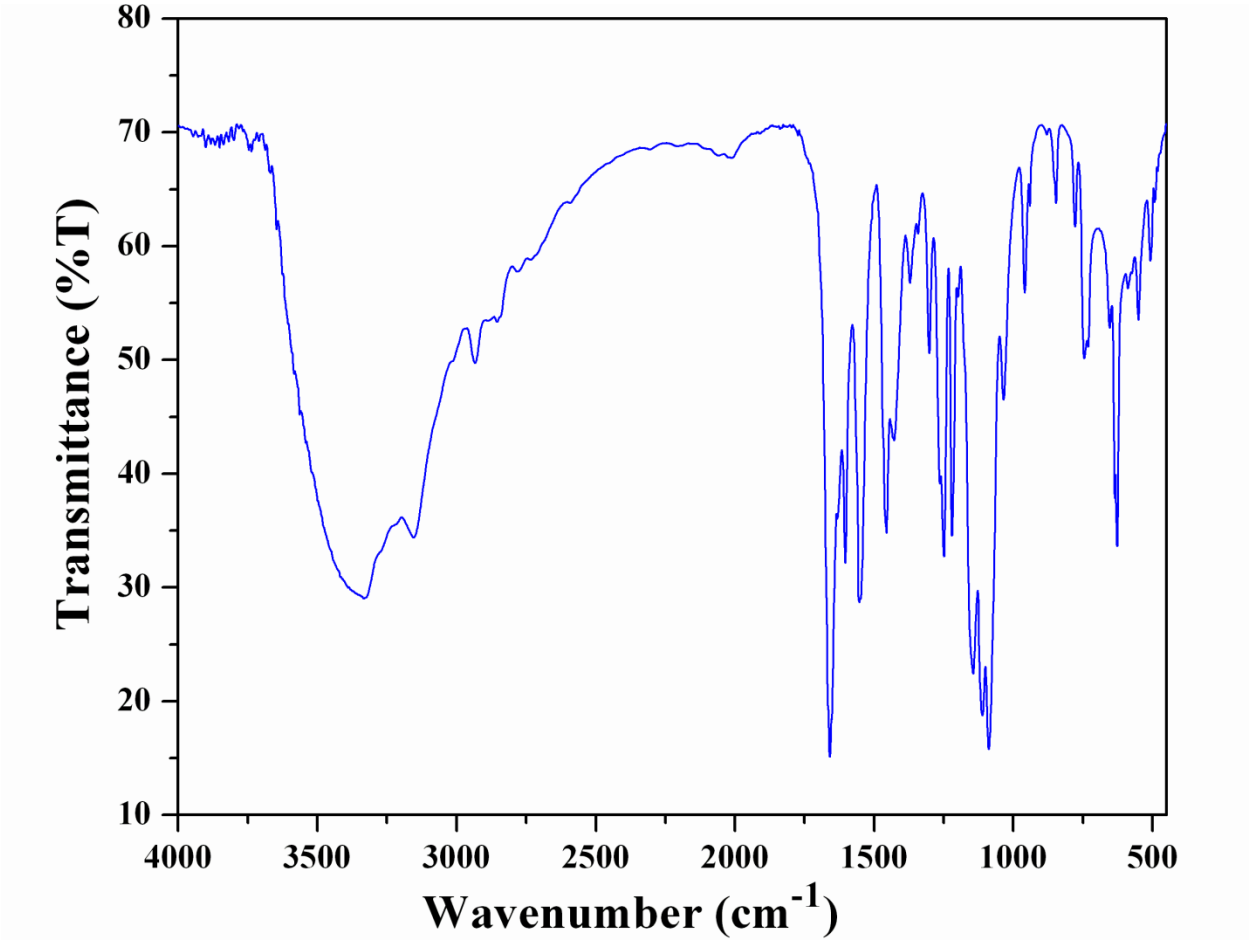


**Figure S7**: IR spectrum (450-4000 $cm^{-1}$) of the complex.

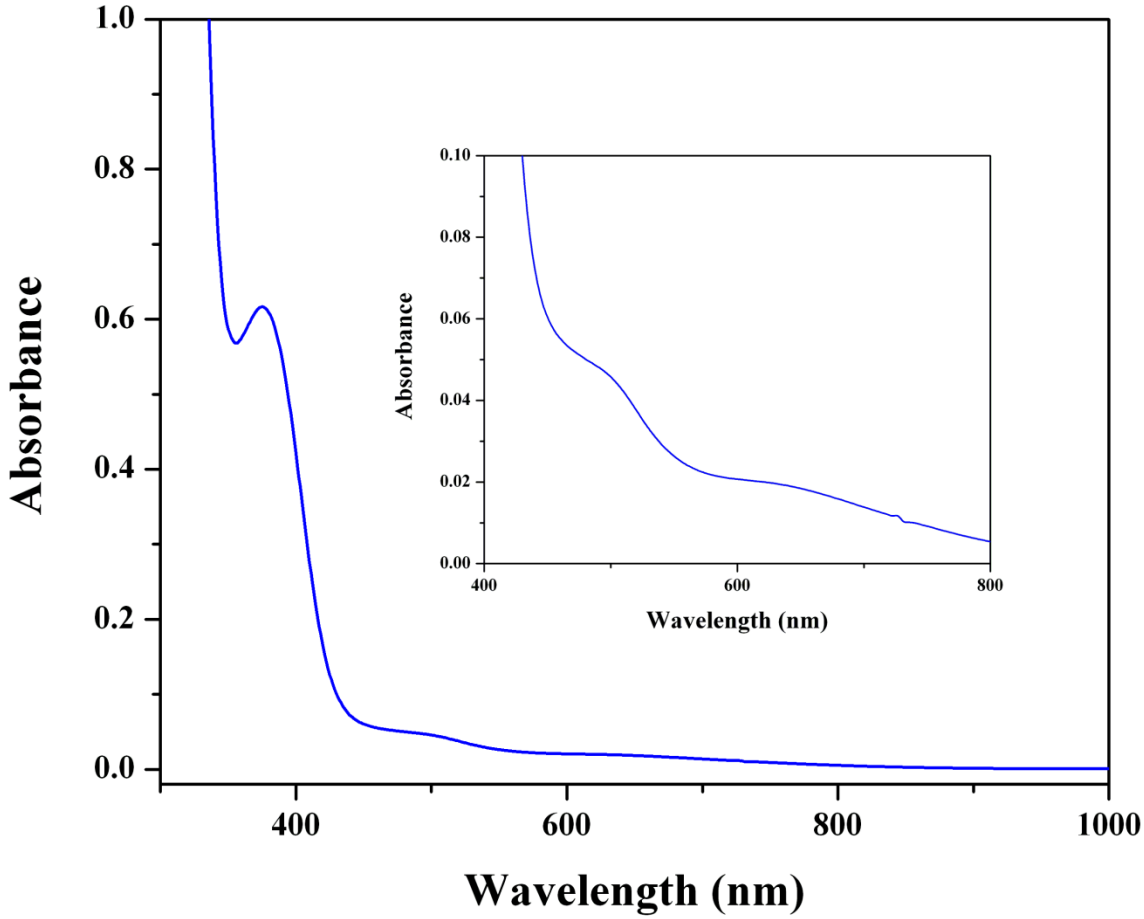


**Figure S8**: The absorption spectrum of the complex in acetonitrile medium.

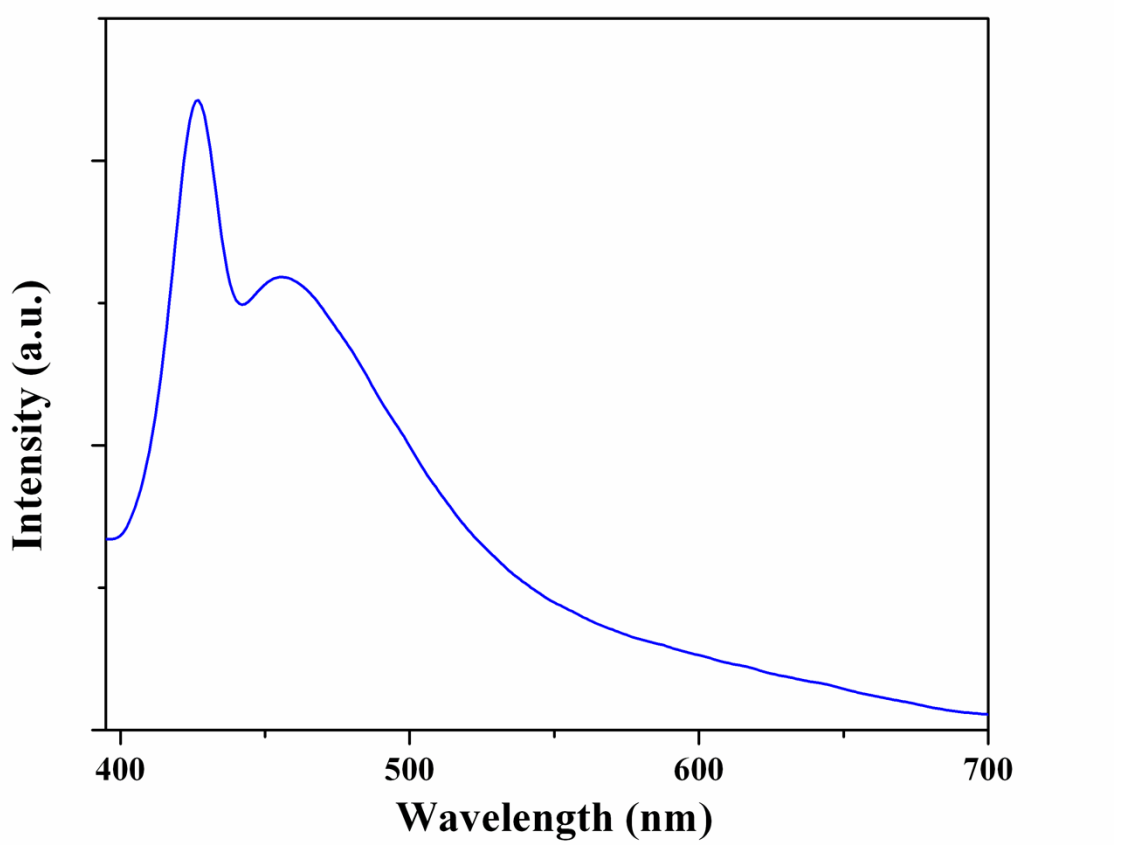


**Figure S9:** Photoluminescence spectrum of the complex in acetonitrile at room temperature.

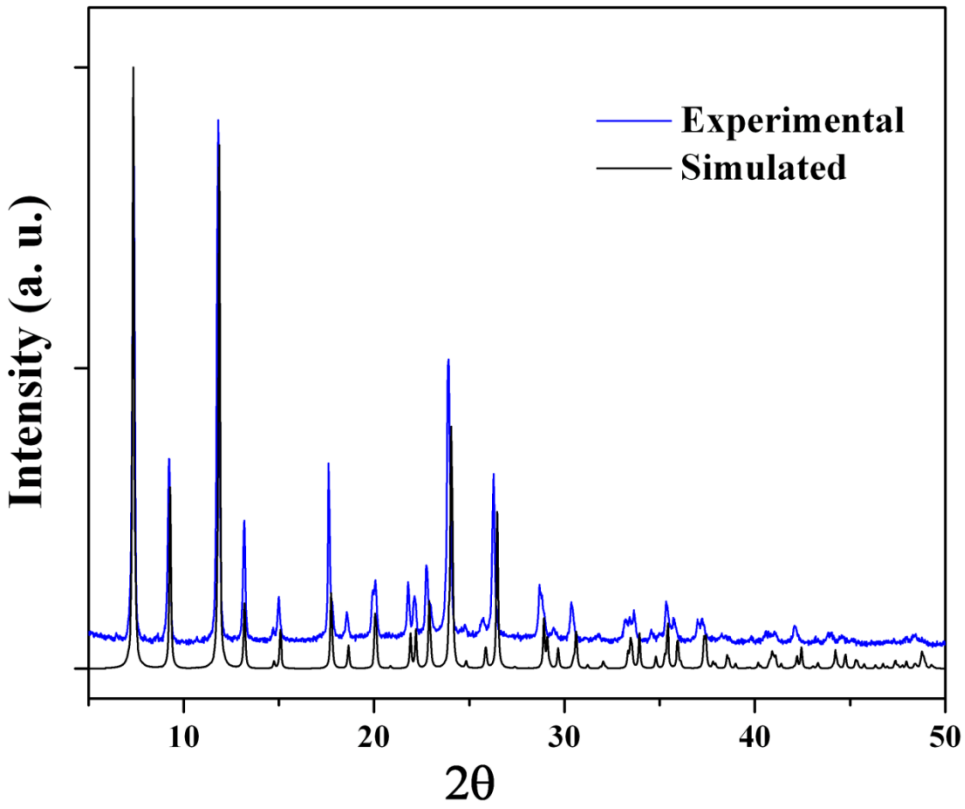


**Figure S10:** Experimental and simulated powder XRD patterns of the complex.